JOURNAL OF CATALYSIS **173,** 383–398 (1998)
ARTICLE NO. CA971916

Structure/Function Relationships in MgO-Doped Nd_2O_3 Catalysts for the Methane Coupling Reaction

Andrew Burrows,*[,1] Christopher J. Kiely,* Justin S. J. Hargreaves,† Richard W. Joyner,† Graham J. Hutchings,‡ Mikhail Yu. Sinev,§ and Yurii P. Tulenin§

*Department of Materials Science and Engineering, University of Liverpool, Liverpool, Merseyside, L69 3BX, United Kingdom; †Catalysis Research Laboratory, Nottingham Trent University, Clifton Lane, Nottingham, NG11 8NS, United Kingdom; ‡Leverhulme Centre for Innovative Catalysis, University of Liverpool, Liverpool, Merseyside, L69 3BX, United Kingdom; and §Institute of Chemical Physics, Russian Academy of Sciences, Kosygina St. 4, Moscow 117334, Russia

Received June 10, 1997; revised September 23, 1997; accepted September 23, 1997

The work presented in this paper extends a previous study of catalysts based on mixtures of MgO and Nd_2O_3 used in the oxidative coupling of methane (OCM) reaction. MgO-doped neodymia catalysts have been prepared by two different methods with various MgO loadings and their methane coupling performance compared with that of pure Nd_2O_3. Quite dramatic differences in catalytic performance have been observed between catalysts prepared by coprecipitation (Series A) and impregnation (Series B). Particularly striking is the highly beneficial effect on activity and C_2 selectivity that the addition of 10 at.% MgO has on the Series B material. In both cases catalytic performance was related to the structural form of the material. Structural details for these catalysts have been obtained from high-resolution electron microscopy observations and powder X-ray diffraction. The results show that the microstructure of pure Nd_2O_3 is significantly different depending on the preparation route: Series A material contains Nd_2O_3 in various states ranging from areas having a high degree of crystallinity to extensive regions of semicrystalline/disordered material, whereas Series B Nd_2O_3 was almost exclusively in the hexagonal form. In general, MgO-doped neodymia catalyst materials have also been found to contain a complex mixture of Nd_2O_3 phases which for Series B materials became apparent after adding up to 3 at.% MgO. With a scanning transmission electron microscope, it has been determined that Mg^{2+} dissolution into the neodymia (up to 2.5 at.%) almost certainly takes place. This result in particular may explain the synergistic effect observed for OCM catalysts of this type.

1. INTRODUCTION

The large reserves of natural gas that currently exist have prompted research groups worldwide to investigate using CH_4 as an alternative feedstock. Thus the oxidative coupling of methane (OCM) to form ethane and ethene has been studied extensively over the years and can be accomplished with a wide variety of oxide catalysts (1). The desired OCM reactions are

$$2CH_4 + \tfrac{1}{2}O_2 \rightarrow C_2H_6 + H_2O,$$

$$2CH_4 + O_2 \rightarrow C_2H_4 + 2H_2O.$$

These reactions are generally considered to occur by initial homolytic cleavage of the CH_4 molecule at the surface of the catalyst, followed by subsequent gas-phase recombination of methyl radicals to form the desired C_2 products. However, in oxidation catalysis the possibility of total oxidation is always present, so the following unselective reactions are also likely to occur:

$$CH_4 + \tfrac{3}{2}O_2 \rightarrow CO + 2H_2O,$$

$$CH_4 + 2O_2 \rightarrow CO_2 + 2H_2O.$$

Hence the goal of OCM catalyst design is to achieve good CH_4 conversion whilst at the same time maintaining a high selectivity for the desired C_2 hydrocarbons. There have been many studies concerning active catalyst formulations and the reaction mechanism of conversion, whereas relatively few attempts have been made to relate catalytic performance with the morphology of the catalyst.

We have pursued the structure sensitivity aspect of OCM catalyst design for MgO and doped MgO catalysts for a number of years. By comparing the microstructure and performance of pure MgO catalysts prepared by a number of very different routes, we have demonstrated that the selectivity and specific catalytic activity are unaffected by the number of corner or edge sites that the MgO exposes (2). This suggested that vacancies on the planar {100}-type surfaces of MgO are likely to be active sites for methane activation. We have also shown that the addition of lithium carbonate to MgO results in subtle changes in the surface structure (3). The improved catalytic performance of Li-doped MgO first observed by Ito and Lunsford (4) was

[1] To whom correspondence should be addressed. Fax: 0151-794-4675. E-mail: ab0895@liv.ac.uk.

0021-9517/98 $25.00

associated with, amongst other effects, the presence of dislocations creating active sites on the MgO surface.

More recently (5, 6) we have described how the addition of neodymia to MgO also has a beneficial effect on the activity and C_2 selectivity. It was established (7, 8) that the extent of the synergistic effect depended critically on the morphology of the neodymia. Six distinct neodymia morphology types were identified in two series of catalysts prepared by impregnation and coprecipitation:

i. Extended crystalline thin films of Nd_2O_3
ii. Cubic and hexagonal "bulk" Nd_2O_3 crystals supported on MgO
iii. Large isolated hexagonal Nd_2O_3 needles
iv. Small epitaxial microclusters 1–2 nm in size
v. Continuous disordered neodymia thin films
vi. Individual clusters containing only one to three molecules.

After careful correlation of catalytic performance with the morphological form of Nd_2O_3 present, it was apparent that bulk neodymia phases did not contribute significantly to the observed increase in catalytic performance. This disordered neodymia films were deduced to be the source of synergy for the Nd_2O_3-on-MgO catalysts. High-spatial-resolution chemical microanalysis studies [using scanning transmission electron microscopy (STEM)] of the two series of catalysts indicated that Nd^{3+} ions did not penetrate into the MgO support. It was speculated that the high efficacy of the mixed $MgO–Nd_2O_3$ catalysts is due to the partial substitution of Nd^{3+} cations by Mg^{2+} in the glassy thin films and the corresponding formation of active anion–radical species, O^-, caused by charge-compensation effects (5, 6).

In this paper we extend these studies to the "reverse" system where Nd_2O_3 catalysts are doped with MgO, again to ascertain structure/reactivity relationships. A similar methodology has also been employed, by preparing catalysts via coprecipitation and impregnation routes and comparing methane coupling performance with that of a pure standard, i.e., Nd_2O_3. STEM microanalysis has again been employed to determine whether or not there is dissolution of Mg^{2+} into any of the neodymia morphologies.

2. EXPERIMENTAL

2.1. Catalyst Preparation

Two series of MgO-doped neodymia catalyst samples of increasing magnesium oxide loading, i.e., 0.0, 0.5, 1.0, 3.0, and 10.0 at.%, were prepared. Series A catalysts were coprecipitated as the mixed hydroxide from a mixed nitrate solution using ammonium hydroxide; the slurry evaporation technique was used. An undoped Nd_2O_3 standard sample for this series was obtained similarly as the pure neodymia salt from a neodymium nitrate solution.

Series B samples were prepared by impregnation of pure Nd_2O_3 with MgO using aqueous magnesium nitrate, whilst a pure neodymia sample for direct comparison was obtained by treating pure Nd_2O_3 with water, then drying the residue. The reason for adopting this latter procedure is because we have previously found that water-treated magnesium oxide catalysts, derived from magnesium hydroxide and magnesium hydroxycarbonate, differed significantly in terms of morphology with respect to their source materials (2). All Series A and B materials were calcined in air at 850°C for 6 h prior to catalytic testing and microstructural analysis and stored carefully in sealed glass containers.

2.2. Catalyst Testing

The catalytic results were obtained using similar apparatus as described previously for neodymia-doped MgO catalysts (5, 6). A standard laboratory microreactor was loaded with 0.01 g of catalyst and pretreated in air as the temperature was raised to 600°C, then exposed to a gas mixture of methane, oxygen, and nitrogen in the ratio 50 : 10 : 40. The gas flow rate was varied to maintain low degrees of conversion of O_2 and CH_4 (of less than 15 and 3%, respectively). These conditions were chosen in order to measure the initial rates of methane coupling and total oxidation when the consecutive oxidation of C_2 hydrocarbons (mainly ethane) could be neglected. Reaction temperatures reported for Series A and B samples are different (650 and 600°C, respectively) because of the great difference in their catalytic performance.

2.3. Microstructural Characterisation

Precise crystallographic details for the two components of this system, atomic positions and space group information, have been described elsewhere (8). Magnesium oxide adopts the cubic sodium chloride-type structure with a lattice parameter of 0.42 nm. Neodymium oxide, Nd_2O_3, is a rare earth sesquioxide that is isostructural with La_2O_3. It can exist in either hexagonal or cubic polymorphic form (9). The hexagonal phase has $a = 0.383$ nm and $c = 0.599$ nm and contains one molecular unit per unit cell. The cubic form of Nd_2O_3 has a lattice parameter of 1.1048 nm and contains 16 molecular units per unit cell. As in our previous paper (8), we specify the planes and zone axes of the hexagonal Nd_2O_3 crystal system using a primitive unit cell and the three digit (hkl) Miller index convention.

Two techniques have been used extensively in the microstructural characterisation of the postreactor MgO-doped neodymia samples, namely, electron microscopy and powder X-ray diffraction (XRD). Transmission electron microscopy studies were carried out in a JEOL 2000EX high-resolution microscope operating at 200 kV. Samples were prepared for examination in the transmission electron microscope by dispersing the powder in ethanol and applying a small drop of slurry to a lacey carbon-coated copper

grid. Lattice fringe patterns from individual particles were then analysed by Fourier transform (FT) techniques using the NIH-image software package. Local composition analysis from high-resolution energy dispersive X-ray spectra was obtained using a VG HB601 UX scanning transmission electron microscope. The probe size of this microscope is approximately 1 nm, giving high spatial resolution and a detection efficiency of the order of 0.1 at.%. A Hiltonbrooks modified Philips 1050 powder diffractometer with a copper $K\alpha$ X-ray source was used for the powder X-ray diffraction studies. To minimise the problem of preferred orientation effects when packing the sample for analysis, the sample was sprinkled onto a Vaseline-coated glass slide.

3. RESULTS

3.1. Catalytic Performance

Different methods of introducing magnesia into the Nd_2O_3 produce different effects on the catalyst surface area. Table 1 shows that there is no discernible surface area trend when the MgO content of the catalysts is increased by coprecipitation from zero to 10 at.%. On the other hand, Table 2 indicates that the impregnation route results in a monotonic increase, with the surface area tripling from 1.6 to 4.5 $m^2\ g^{-1}$ as the MgO content of the catalyst increases.

The performance of the two series of catalysts for the oxidative coupling of methane has been studied, and the results are presented in Tables 1 and 2. Temperatures and space velocities have been chosen to satisfy differential conversion criteria, with methane conversions kept to <3% and oxygen conversion ca. <15%. The impregnated catalysts show greater activity than the coprecipitated materials and, because of this, were tested at 600°C, compared with 650°C for the coprecipitated series. The measurements indicate that the specific activities recorded are similar for the two series of catalysts, despite the 50°C difference in testing temperature. Tables 1 and 2 also show that for the coprecipitated materials there is no clear relationship between specific activity and magnesia content, whereas a marked increase in specific activity for the impregnated series occurs only at 10 at.% magnesia loading.

TABLE 1

Catalytic Performance of Series A Catalysts (Coprecipitated) at 650°C

at.% MgO	Surface area ($m^2\ g^{-1}$)	Specific activity for CH_4 conversion ($10^5\ mol^{-2}\ s^{-1}$)	C_2 selectivity (%)
0	2.5	2.3	0.8
0.5	1.9	1.3	2.4
1.0	1.7	1.6	3.1
3.0	2.2	1.2	4.2
10.0	1.6	2.5	8.2

TABLE 2

Catalytic Performance of Series B Catalysts (Impregnated) at 600°C

at.% MgO	Surface area ($m^2\ g^{-1}$)	Specific activity for CH_4 conversion ($10^5\ mol^{-2}\ s^{-1}$)	C_2 selectivity (%)
0	1.6	1.1	3.1
0.5	2.4	1.2	4.4
1.0	2.8	1.6	6.2
3.0	4.2	1.4	11.6
10.0	4.5	3.7	21.5

The tables show that for both series of catalysts the combined selectivity to C_2 hydrocarbons (ethane + ethene) increases roughly tenfold for Series A and sevenfold for Series B materials, respectively, over the range of magnesia contents. Taken together with the much smaller changes in activity, the selectivity results suggest that the introduction of magnesia replaces some neodymia sites, which are active only in the total oxidation of methane, with selective sites of similar activity that produce methyl radicals as the first step in methane coupling. It was therefore of interest to study both series of materials by transmission electron microscopy, with the aim of establishing structure–performance relationships.

3.2. Microstructure: Pure Series A

A low-magnification micrograph of pure Nd_2O_3 obtained from the pure Series A material is shown in Fig. 1a. The sample is found to contain large irregularly shaped platelike particles with typical lateral dimensions between approximately 50 and 900 nm. When these particles are viewed at higher magnification, as shown in Fig. 1b, the neodymia microstructure is revealed as a complex mixture of phases, including large disordered/semicrystalline areas (labelled x) and smaller patches of highly ordered crystalline material (labelled y). The highly ordered crystalline areas have dimensions in the range 1.5 to 25 nm in diameter. Analysis of many lattice fringe patterns has allowed us to identify the presence of the cubic and hexagonal forms of Nd_2O_3 as well as some neodymium hydroxide, $Nd(OH)_3$. Crystalline cubic areas are the most common and extensive whilst for the latter two cases, the areas occupied are usually only a few nanometers in diameter. A good example of an extended area of cubic Nd_2O_3 is shown in Fig. 2a and has been identified as being consistent with the [010] projection (as deduced from the FT and theoretical diffraction pattern shown in Figs. 2b and 2c, respectively). The change in lattice fringe contrast across the crystalline area of Fig. 2a simply arises due to a variation in thickness across the grain.

An unusually large crystalline area of the hexagonal form of Nd_2O_3 (roughly 12 nm in size) is shown in Fig. 3a.

FIG. 1. (a) Low-magnification image of Series A undoped Nd_2O_3. (b) The complex microstructure at higher magnifications: x, disordered/semi-crystalline material; y, highly ordered crystalline material.

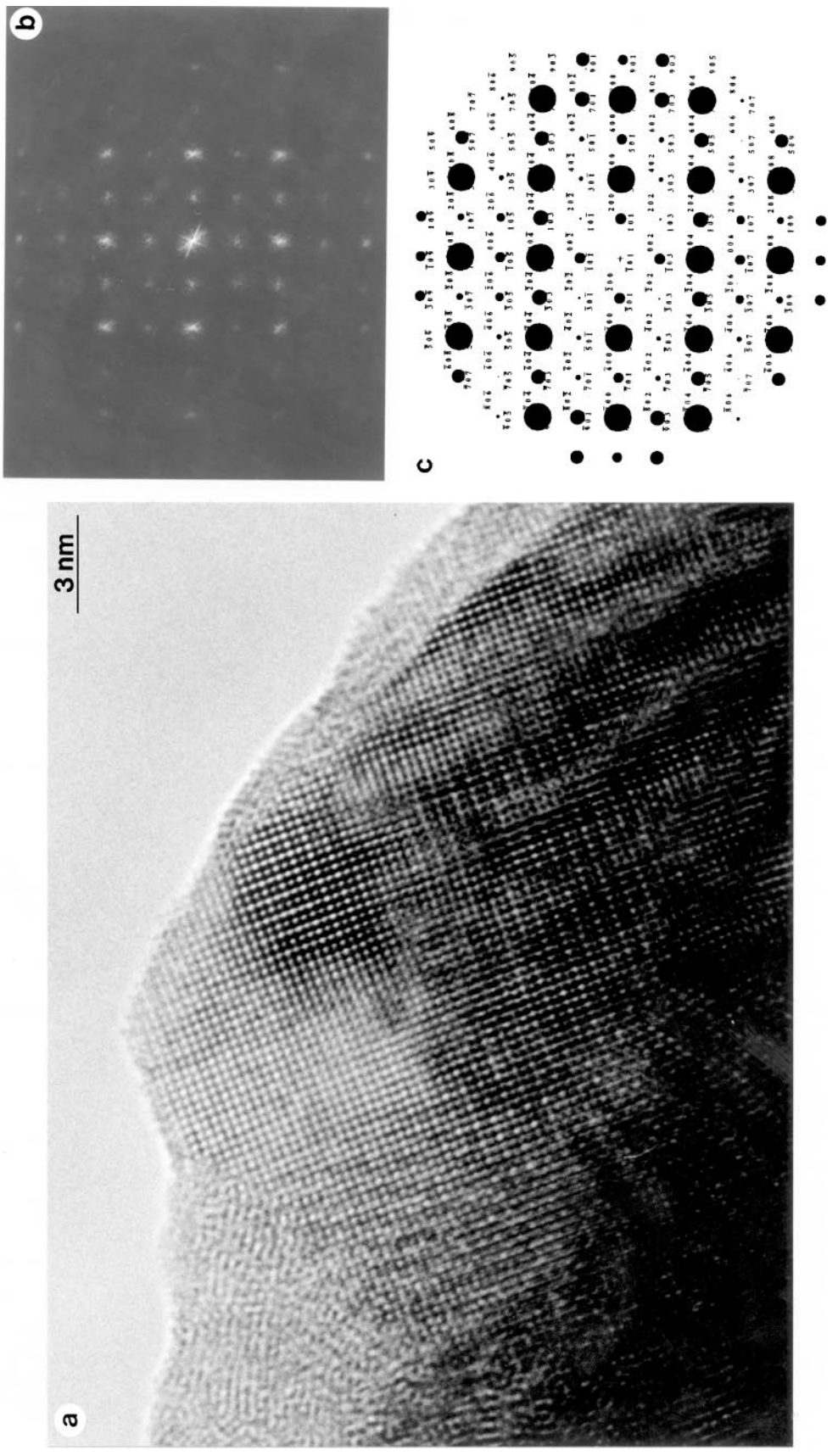

FIG. 2. Lattice image (a) and corresponding FT (b) of a cubic area of Nd_2O_3 oriented along the [010] zone axis. (c) Simulated cubic [010] diffraction pattern.

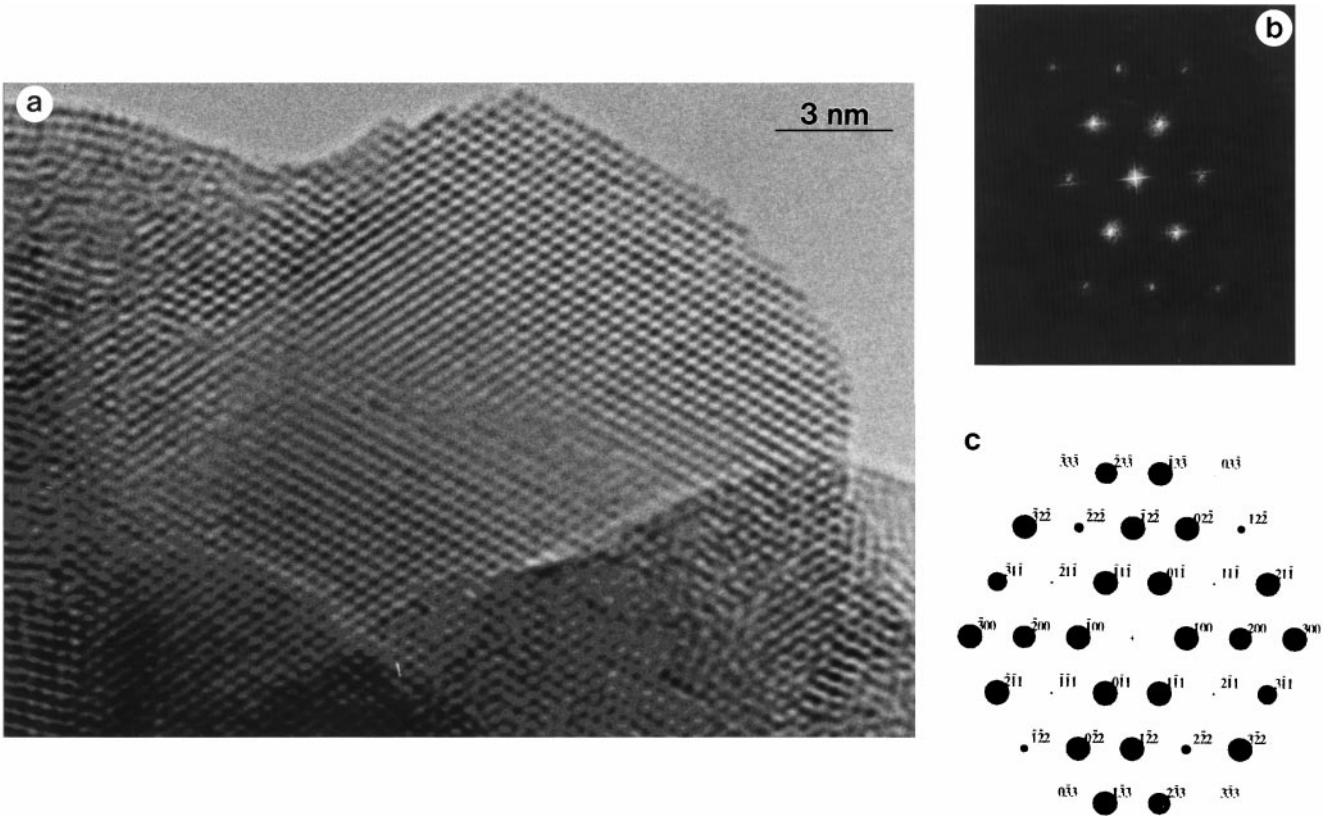

FIG. 3. Lattice image (a), corresponding FT (b), and model diffraction pattern (c) of hexagonal neodymia oriented along the [011] zone axis.

The fringe structure within this region is consistent with hexagonal Nd_2O_3 projected down the [011] zone axis, as shown by the corresponding FT from the image and indexed model diffraction pattern for the [011] hexagonal direction (Figs. 3b and 3c, respectively).

It was interesting to note that whenever the $Nd(OH)_3$ phase was found, there was usually an adjacent region of cubic Nd_2O_3 in the same grain as shown in Fig. 4a. The respective phases are indicated on the micrograph and in the case of $Nd(OH)_3$, the fringe structure corresponds to a projection along the [211] zone axis [$Nd(OH)_3$ possesses a hexagonal UCl_3-type crystal structure, space group number 176 (10)]. The FT and model diffraction pattern for this direction are shown in Figs. 4b and 4c, respectively. Conversely, crystalline regions of hexagonal Nd_2O_3 were never found in close proximity to areas of $Nd(OH)_3$.

Powder XRD patterns were also recorded for this material; a typical example is shown in Fig. 5. The reflections in Fig. 5 have been indexed in Table 3 to show the possible reflecting planes from the following three phases that could give rise to a particular peak: cubic and hexagonal Nd_2O_3 and neodymium hydroxide, $Nd(OH)_3$. However, the match is not precise due to the high degree of overlap between the respective plane spacings. Since in the electron microscope the constituent particles appear platelike, precise comments about the relative proportions of the three crystalline phases derived from peak intensities cannot be made. This is due to preferred orientation effects which may still be present in the XRD patterns, despite the steps taken to minimise them.

TABLE 3

Possible Reflecting Planes and Corresponding *d* Spacings for Cubic Nd_2O_3, Hexagonal Nd_2O_3, and Neodymium Hydroxide, $Nd(OH)_3$

		Possible reflecting planes—spacing (Å)		
Peak	*d* spacing (Å)	Cubic Nd_2O_3	Hexagonal Nd_2O_3	$Nd(OH)_3$
1	5.570	(002)—5.528		(100)—5.570
2	3.210	(100)—3.200		(110)—3.200
3	3.100	(222)—3.192		(101)—3.080
4	2.789	(400)—2.772		(200)—2.768
5	2.445			(111)—2.450
6	2.234		(102)—2.225	
7	2.109	(510)—2.174		(210)—2.092
8	1.851			(300)—1.848
9	1.830			(211)—1.842
10	1.773	(611)—1.797		
11	1.617		(112)—1.614	
12	1.592		(201)—1.599	(220)—1.605
13	1.550	(710)—1.565		(310)—1.540
14	1.427			(311)—1.417
15	1.391	(732)—1.407		(400)—1.392
16	1.319	(653)—1.324		(401)—1.311

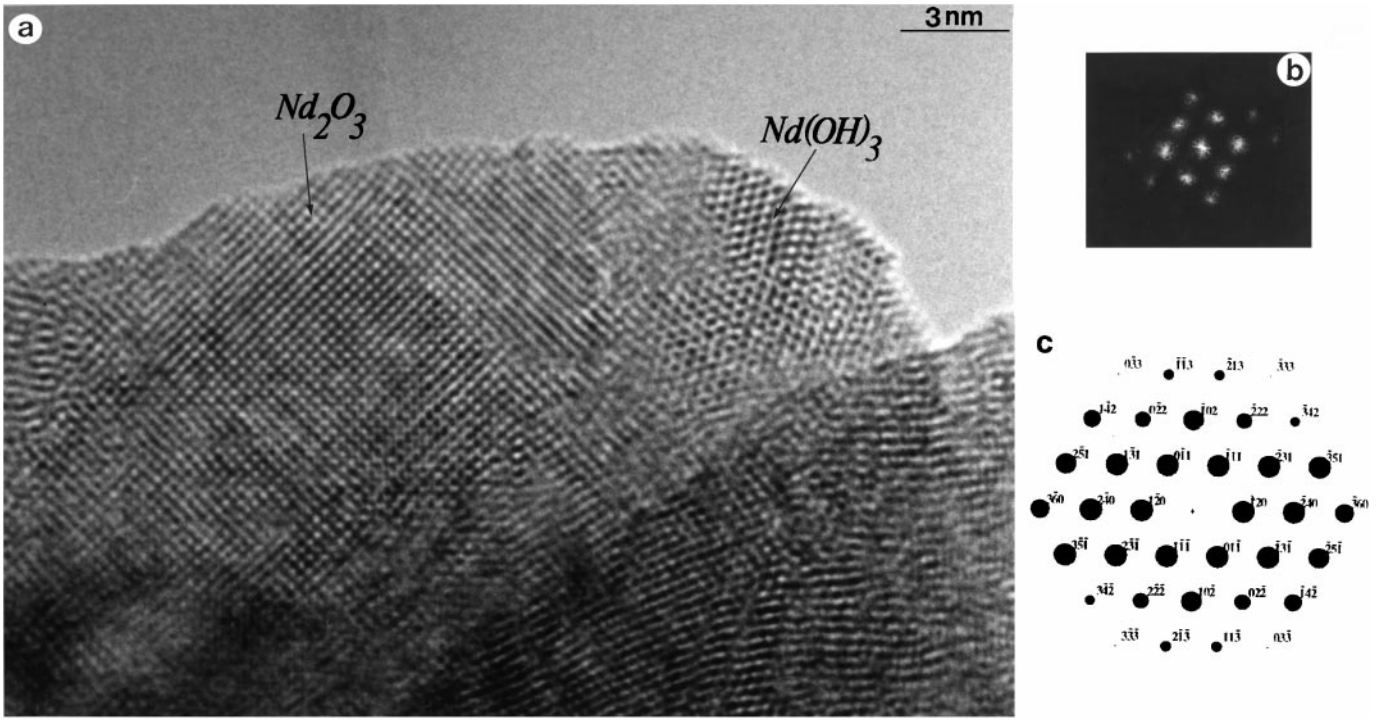

FIG. 4. (a) HREM image of an area of $Nd(OH)_3$ oriented along the [211] zone axis in close proximity to cubic Nd_2O_3. (b) FT and (c) model diffraction pattern of the $Nd(OH)_3$ [211] zone axis.

At this point it is worth discussing possible reasons for the observed complex microstructure, in particular the extensive regions of disorder. Bernal *et al*. (11–13) have investigated the chemistry of lanthanide sesquioxides aged in air, i.e., exposed to atmospheric water and carbon dioxide at ordinary temperatures and pressures. These studies have shown that the ageing process takes place at different rates for the cubic and hexagonal forms of Nd_2O_3, the latter being more stable (13), giving rise to bulk hydration indicated by the presence of $Nd(OH)_3$ and carbonation products. Significantly, it was noted that XRD alone was not the ideal technique for establishing the precise nature of the carbonation products (11). Using high-resolution electron microscopy (HREM) these authors demonstrated that hydrated and carbonated samarium oxide, which is isostructural with Nd_2O_3, was significantly disordered in the bulk (12). Thus, given the presence of $Nd(OH)_3$ and the disorder observed within Sample A, it would appear that the material has hydrated/carbonated at some stage, presumably during reaction (this point will be dealt with in greater detail in Section 4). Hence, the complex microstructure we observe will hereafter be referred to as hydrated Nd_2O_3. The greater stability of hexagonal Nd_2O_3 toward hydration and carbonation effects as determined by Bernal *et al.* seems to be borne out by our observation that $Nd(OH)_3$ was never found in close proximity to crystalline regions of hexagonal neodymia.

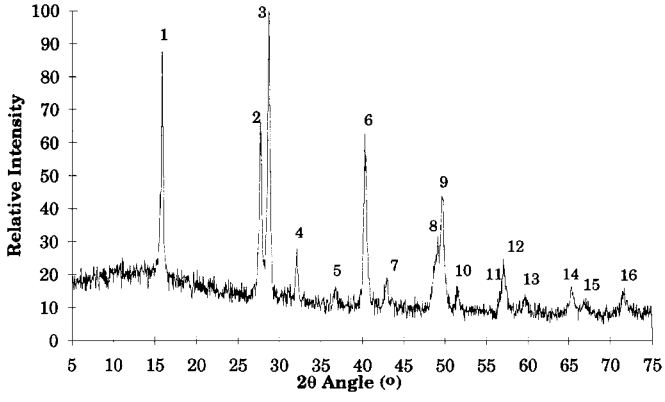

FIG. 5. XRD pattern given by undoped Series A Nd_2O_3.

3.3. Microstructure: Pure Series B

The XRD pattern obtained from pure neodymia prepared by impregnation (Fig. 6) matches almost exclusively the hexagonal form of Nd_2O_3 (the specific hexagonal neodymia reflections are indicated on the figure). The low background signal and the sharpness of the reflections indicate a high degree of crystallinity. There are also weak reflections in this profile from the hydrated form of Nd_2O_3, suggesting trace amounts of this material are also present. Figure 7 is a typical low-magnification micrograph from

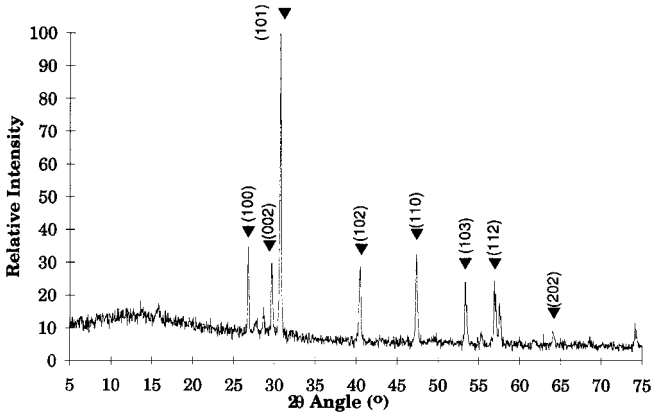

FIG. 6. XRD pattern given by undoped Series B Nd_2O_3. The labelled peaks correspond to reflections arising from the hexagonal phase of neodymia. Unlabelled peaks correspond to "hydrated" Nd_2O_3 which can be inferred from Fig. 5 and Table 3.

pure Series B material. The particles are generally spherical although more angular ones have been observed and their lateral size varies between 200 and 400 nm. A typical lattice image fringe pattern from a Series B particle is shown in Fig. 8a. The corresponding FT (Fig. 8b) displays a good match to the indexed model diffraction pattern of a [321] hexagonal Nd_2O_3 zone axis (Fig. 8c).

Occasional platelike particles similar to those found in Series A are also present in the sample, such as that labelled z in Fig. 7, with lateral dimensions of the order of 400 nm (comparable to pure Series A grains). At higher magnifications, such regions are seen to exhibit a complex microstructure similar to that of the coprecipitated pure Series A sample which is consistent with the trace hydrated Nd_2O_3 signal obtained in the XRD pattern.

3.4. Microstructure: Doped A Series

XRD patterns from all of the MgO-doped catalysts in Series A were recorded and representative profiles are shown in Fig. 9 [(a) 1 at.% MgO, (b) 10 at.% MgO]. There is an obvious similarity to the patterns obtained from the undoped Series A Nd_2O_3 in terms of peak positions and even the relative intensities (refer to Fig. 5). The profiles have been indexed using the data in Table 3 to show the possible origin of the reflections from the two crystalline forms of Nd_2O_3 as well as $Nd(OH)_3$. The presence of characteristic lines for magnesium oxide could not be detected in this series, even at the highest (10 at.%) MgO loading.

At low magnifications, the constituent particles, like the corresponding pure material, are platelike and highly irregular in shape possessing similar lateral dimensions. At high magnifications, all samples showed the characteristic microstructure of hydrated Nd_2O_3 as indicated in Fig. 10 which was recorded from the sample loaded with 1 at.% MgO. This microstructure is typical for the series as a whole. There is, however, a definite increase in the volume fraction of the disordered phase component as compared with the pure material (i.e., fewer extended regions of highly ordered phases), but this effect is difficult to quantify from HREM images.

Discrete MgO particles within the doped samples were observed only very infrequently in the samples loaded with 3 and 10 at.% MgO. Figure 11, from the catalyst loaded with 3 at.% MgO, shows a discrete magnesium oxide particle having typical dimensions of about 25 nm. A thin disordered surface film of neodymia is present on the MgO surface that is reminiscent of the found in our previous study of the Nd_2O_3-doped MgO catalyst system (7, 8). This is by far the most common neodymia morphology observed on the MgO surface, along with individual Nd_2O_3 clusters.

3.5. Microstructure: Doped B Series

XRD patterns for the Series B catalysts are shown in Figs. 12a through 12d. It is obvious that as the MgO content increases, there is a gradual change from a highly ordered hexagonal structure to a much more complex

FIG. 7. Low-magnification micrograph of pure Series B Nd_2O_3. The grain marked z is an example of the platelike material occasionally seen in this sample.

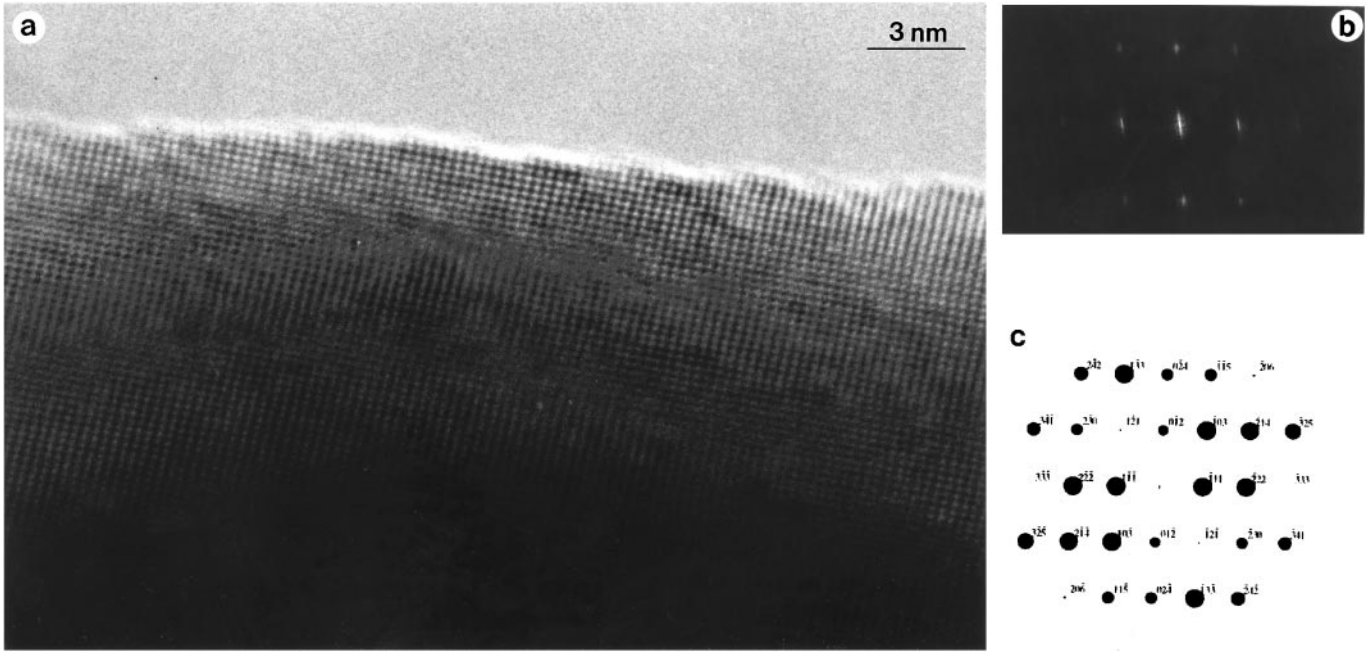

FIG. 8. Lattice image (a) obtained from a pure Series B particle. Corresponding FT (b) and model diffraction pattern (c) of the [321] hexagonal Nd_2O_3 zone axis.

hexagonal/cubic/hydrated oxide mixture similar to that found in samples from Series A. The change appears to be complete at a loading of about 3 at.% MgO, at which point the XRD pattern becomes almost indistinguishable from those shown in Fig. 9 of doped Series A catalysts. As with the Series A catalysts, characteristic magnesium oxide reflections were absent from all of the XRD patterns.

Electron microscopy observations of Series B catalysts have proved to be consistent with the conclusions derived from the XRD data. The incidence of the characteristic platelike particle morphology of the Series A sample increased at the expense of the more blocky hexagonal morphology as the MgO content increases. At a loading of 3 at.% MgO, the distinctive morphology of pure Series B material had been completely replaced by platelike particles. Higher-magnification micrographs reveal, once again, that the microstructure in the platelike particles is a complex mixture of disordered and crystalline areas containing cubic and hexagonal Nd_2O_3 and $Nd(OH)_3$ to varying degrees. A representative micrograph of the Series B sample loaded with 3 at.% MgO is shown in Fig. 13.

Discrete magnesium oxide particles ranging from 15 to 40 nm in size were observed in the 3 and 10 at.% samples, but not at all in the 0.5 or 1 at.% materials. In general, they

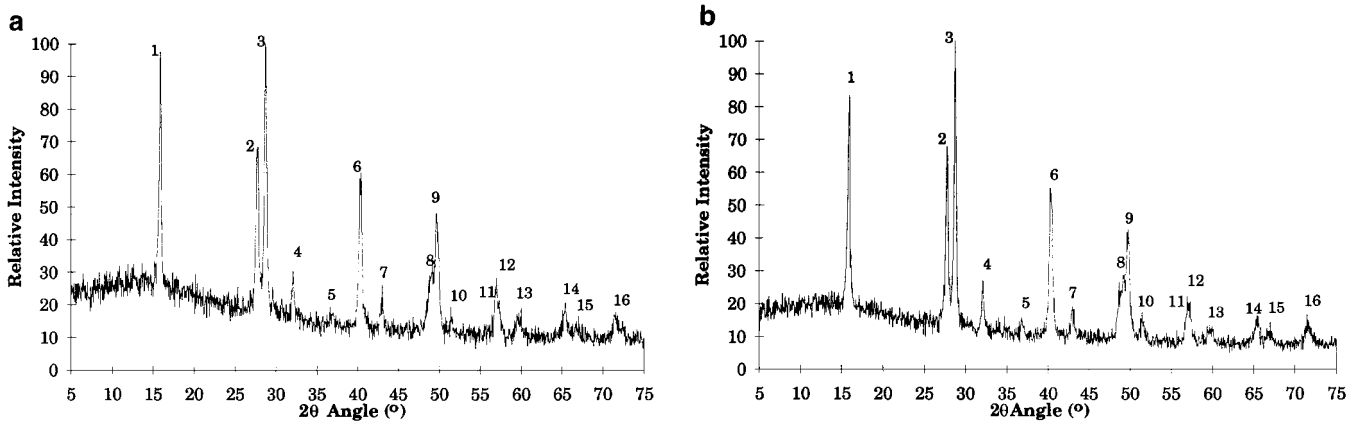

FIG. 9. XRD patterns given by doped Series A catalysts: (a) 1 at.% MgO, (b) 10 at.% MgO.

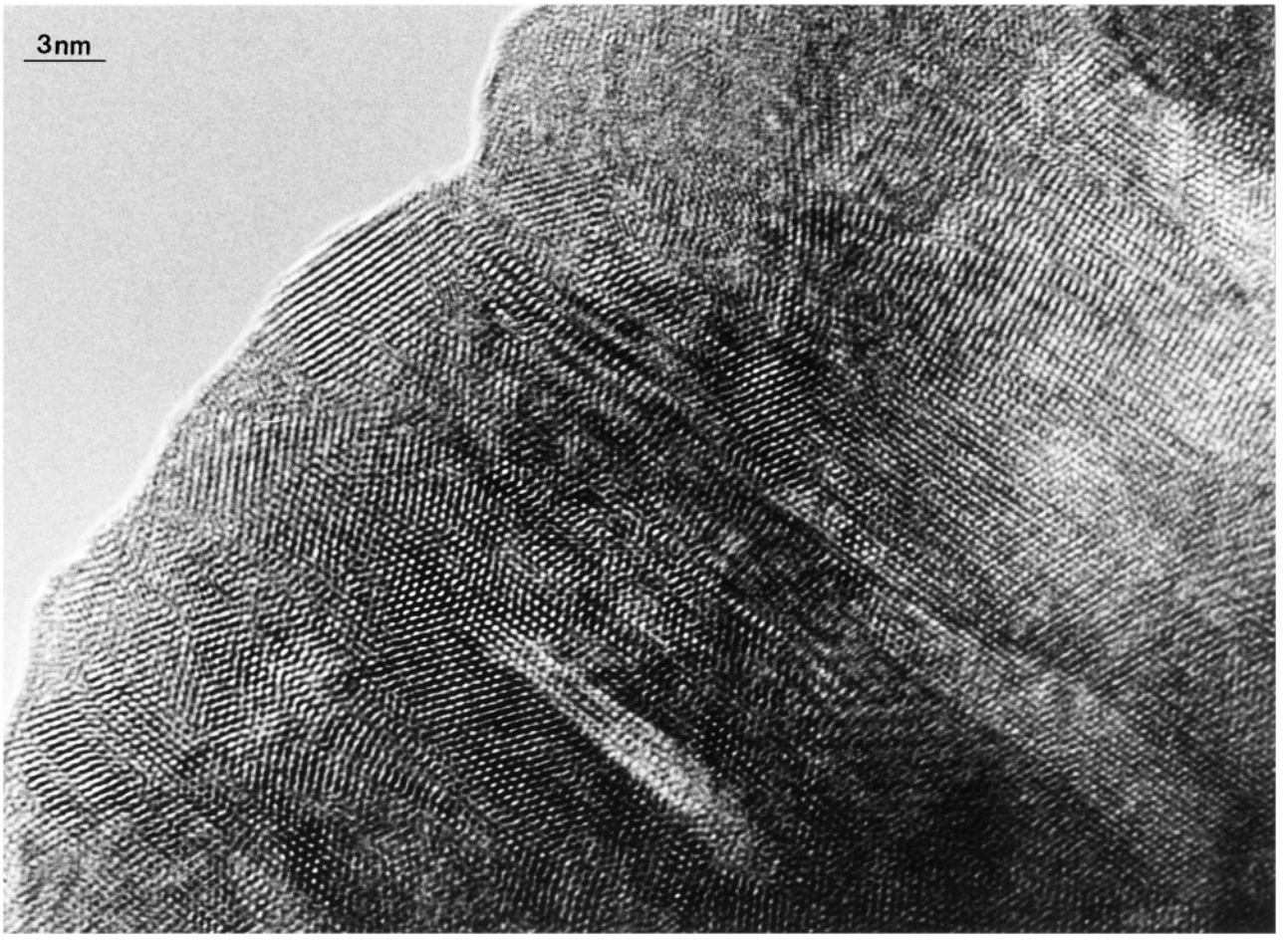

FIG. 10. HREM image obtained from the sample loaded with 1 at.% MgO.

were larger and more numerous than those observed in the heavily doped Series A catalyst. Figure 14 shows such an MgO particle in the sample doped with 10 at.% MgO. It is very significant for this series that these discrete MgO particles always exhibit the continuous disordered overlayer of Nd_2O_3 on the MgO {100}-type facet surfaces.

3.6. Energy-Dispersive X-Ray Microanalysis of 10 at.% MgO/Nd_2O_3 Samples

We have previously speculated (7, 8) that Mg^{2+} ions may be incorporated within the disordered thin neodymia films and postulated they may be the locus of synergy in the OCM reaction for this type of catalyst. This question has been addressed for the two series of MgO-doped neodymia catalysts using high-resolution energy-dispersive X-ray (EDX) microanalysis in a dedicated scanning transmission electron microscope on the samples loaded with 10 at.% MgO. These particular samples were chosen to maximise our chances of detecting any Mg^{2+} dissolution.

Initial investigations showed that the analysis was inherently difficult due to the three factors: (i) loss of oxygen from the neodymia, (ii) loss of magnesium during spectrum acquisition time, and (iii) significant overlap of the Mg $K\alpha$ peak with the Nd $M\gamma$ peak (they occur at energies of 1.253 and 1.181 keV, respectively). Factors i and ii arise due to "knock-on" displacement radiation damage by the electron beam. A more complete description of the experimental details and the inherent difficulties is given elsewhere (14). A typical EDX spectrum is shown in Fig. 15, which was obtained from a disordered region in the Series A catalyst. Quantitative analysis showed this particular grain of neodymia contains 2.5 at.% Mg^{2+}. The spectrum has been labelled to show the positions of the magnesium $K\alpha$ and Nd $M\gamma$ peaks. It was consistently found that the disordered regions gave the largest Mg^{2+} concentrations, which were always between 0.3 and 2.5 at.%. Conversely, the concentration of Mg^{2+} in crystalline areas was always below 0.3 at.%. Compositional analysis has also been carried out on the thin Nd_2O_3 films on MgO but are inconclusive due to beam spreading effects which lead to a contribution to the Mg^{2+} signal from the MgO support. However, the general conclusion from the microanalysis is that dissolution of magnesium ions has taken place up to a maximum concentration

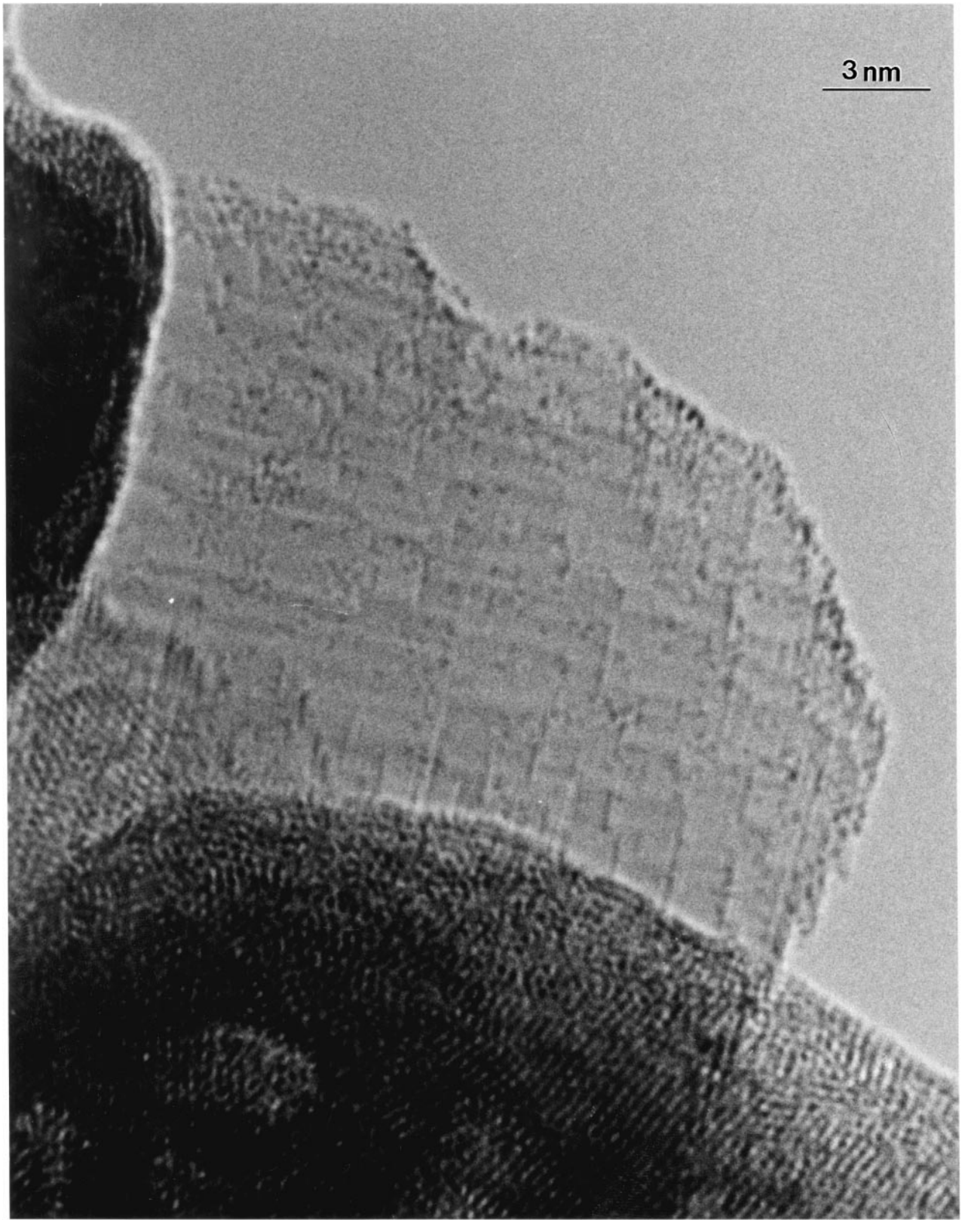

FIG. 11. Discrete MgO particle observed in the 3 at.% MgO Series A catalyst decorated with disordered neodymia.

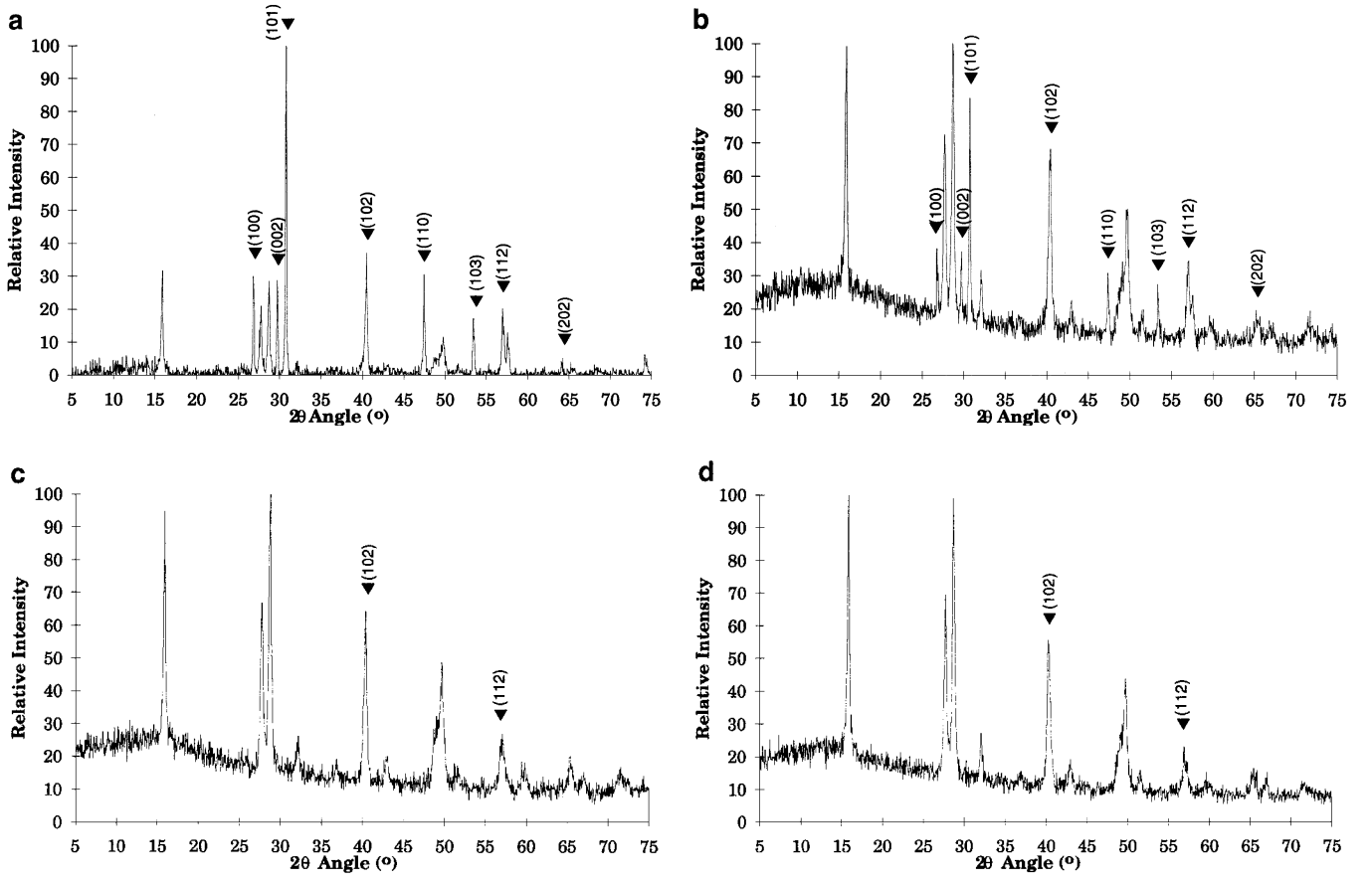

FIG. 12. XRD patterns given by the MgO-doped Series B catalysts: (a) 0.5 at.% MgO, (b) 1 at.% MgO, (c) 3 at.% MgO, (d) 10 at.% MgO. Note the change from an ordered hexagonal pattern to the complex pattern of Series A materials. This is indicated by the reduction in the number of labelled hexagonal neodymia peaks. The unlabelled peaks correspond to those identified for Series A materials (Table 3).

level of approximately 2.5 at.% in both of these samples. It is also reasonable that this incorporation of magnesium ions may be the reason for not observing discrete MgO particles by HREM in the samples doped with 0.5 and 1.0 at.% MgO.

4. DISCUSSION: STRUCTURE/FUNCTION RELATIONSHIPS

In addition to the effects of hydration and carbonation of Nd_2O_3 due to the OCM reaction, a further factor that adds to the complexity of this catalyst system is the polymorphism exhibited by Nd_2O_3. Eyring (15) has comprehensively reviewed the extensive literature on rare earth oxides and their reconstructive polymorphism. The cubic structure of Nd_2O_3 is regarded as metastable, but the range of temperatures over which a particular crystal structure is stable depends significantly on the purity of the starting material. For the case of high-purity Nd_2O_3, Warshaw and Roy (16) found the hexagonal-to-cubic transformation was reversible at around 600°C and that cubic or hexagonal neodymia could be accompanied by its hydrated form depending on the calcination temperature and time, the pressure, and the reactants used. Furthermore, Stecura (17) showed that structural transformations of Nd_2O_3 not only depend on the precursor material but occur over a wide range of temperatures. Thus, consideration has to be given to the possibility that not only has the neodymia hydrated but also that magnesium oxide, acting as an impurity in the neodymia lattice, preferentially stabilises certain neodymia phases. For the Series A catalysts, stabilisation of other phases (not necessarily cubic, but possibly the hydroxide phase and the products of carbonation) by MgO appears to be plausible: the XRD profiles are virtually identical for the whole series and there is a gradual loss of the hexagonal constituent present in the pure material. For Series B catalysts, too, there is a definite trend in converting from a bulk hexagonal crystal structure to the more disordered hydrated Nd_2O_3 form as the MgO concentration increases.

In terms of relating this information to structure/function relationships in this catalyst system, the obvious question to ask is, "Do we believe that what we see is representative of the working catalyst?" If it is accepted that hydration and carbonation have taken place, then is it reasonable to

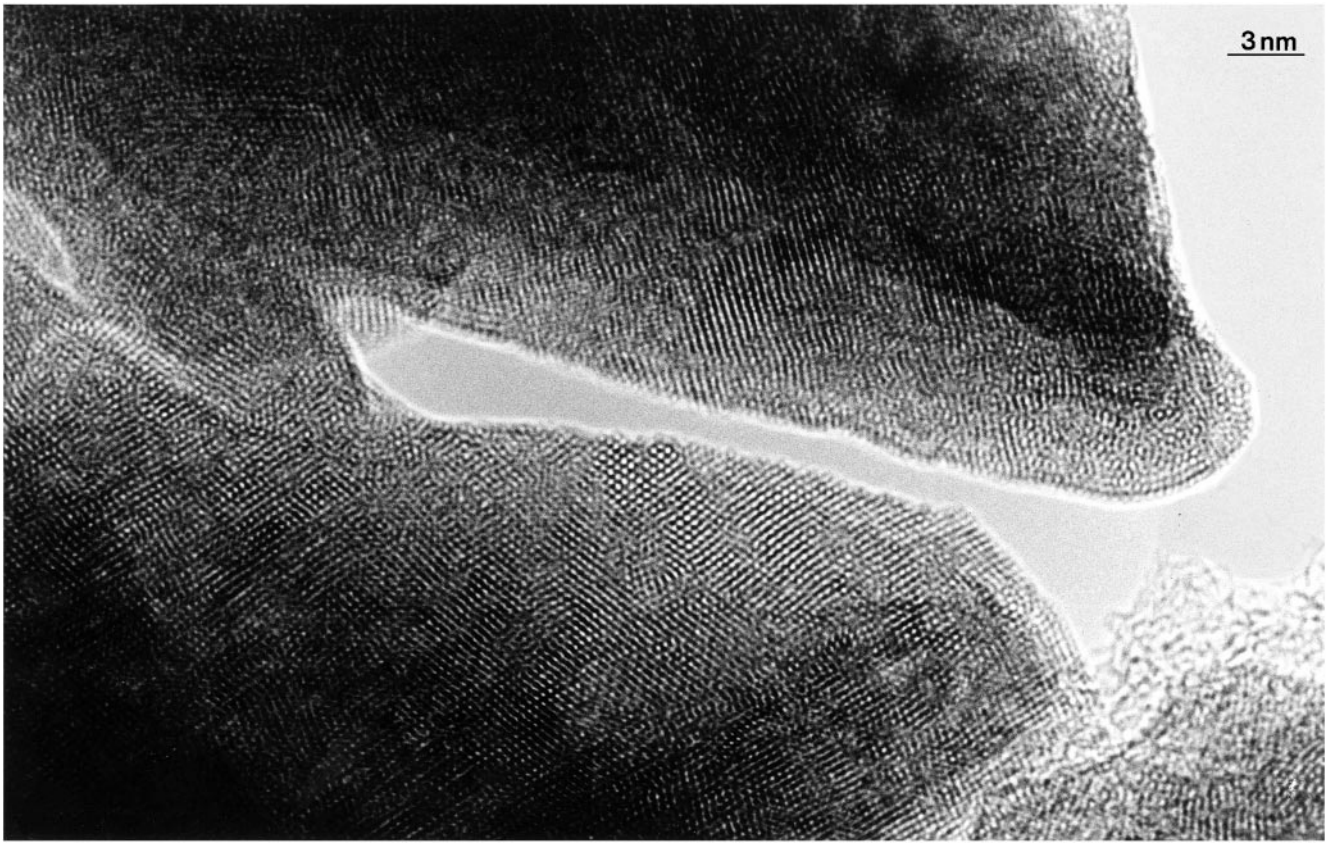

FIG. 13. Representative micrograph obtained from an MgO-doped Series B catalyst.

attempt to correlate the catalytic performance measurements with HREM observations? Significantly, a study of lanthanum oxide in the OCM reaction by Le Van *et al*. (18) revealed, from *in situ* infrared spectroscopy studies, that lanthanum oxycarbonates (of general formula $La_2O_2CO_3$) could be formed during the OCM reaction below 700°C. The stability of these oxycarbonates was found to depend on the preparation conditions of the material: the oxycarbonates in a sample calcined at 800°C for 16 h were found to be less stable than those in a catalyst calcined at 650°C for 2 h. The latter sample also performed better in terms of C_2 selectivity. The presence of multiple phases at these sorts of temperatures has also been noted by Greis (19), who studied hexagonal rare earth sesquioxides and found that temperatures between 1000 and 1600°C had to be employed to decompose all the carbonate contaminants.

Containing both carbon dioxide and steam at high temperature, the OCM reaction mixture is likely to be severely corrosive to any catalyst. We therefore believe that the micrographs are representative of the working catalyst since great care was exercised in storage of the samples between reaction and examination (we cannot of course be certain that atmospheric ageing has been completely prevented, for example, during introduction to the microscope). It is our proposal then that the structural disorder observed in the Nd_2O_3 samples (associated with hydration/carbonation) may well exist under typical reaction conditions and is ultimately beneficial to OCM performance.

Whilst the activities of the two samples of pure Nd_2O_3 are similar, the C_2 selectivity of Series A material is significantly lower. Microstructurally, pure Series A material is composed of platelets containing a complex mixture of disordered neodymia phases, crystalline cubic Nd_2O_3, and lesser quantities of hexagonal neodymia and $Nd(OH)_3$. By contrast, pure Series B neodymia has been shown to be almost completely in the hexagonal form. Therefore, it is apparent that the hexagonal form of neodymia is, overall, a better OCM catalyst than a mixture of ordered cubic and hydrated phases of Nd_2O_3. However, the poor activity and C_2 selectivity values obtained for the pure Series B material concur with our earlier findings (8) that bulk crystalline neodymia phases do not contribute significantly to the catalytic performance of this mixed oxide system.

For the doped Series A catalysts there is a small decrease in specific activity which occurs for all dopant levels except the highest which is similar to the parent material. It is, however, noteworthy that selectivity is improved by the addition of magnesium oxide at all levels studied.

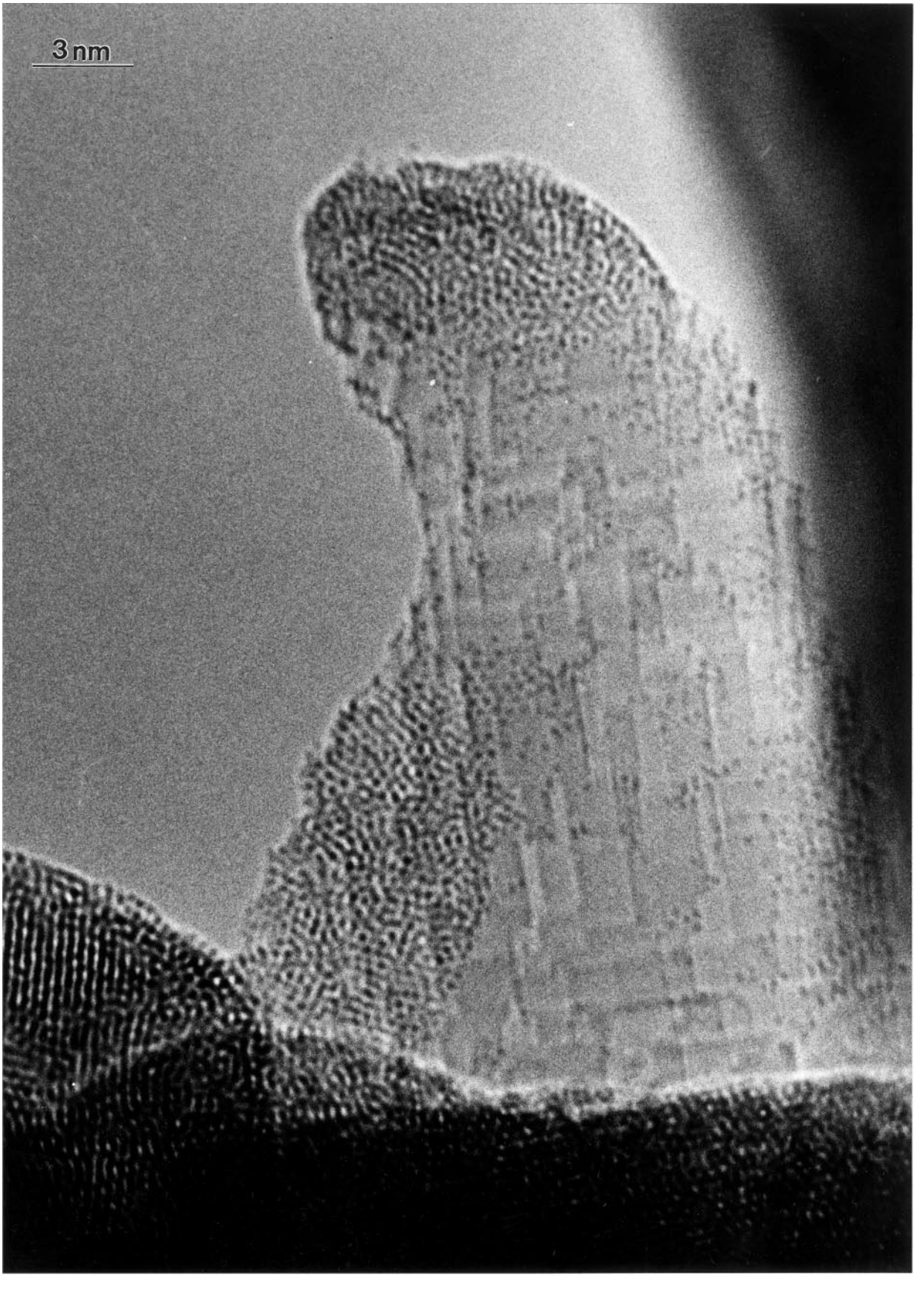

FIG. 14. MgO particle decorated with disordered neodymia observed in the Series B sample loaded with 10 at.% MgO.

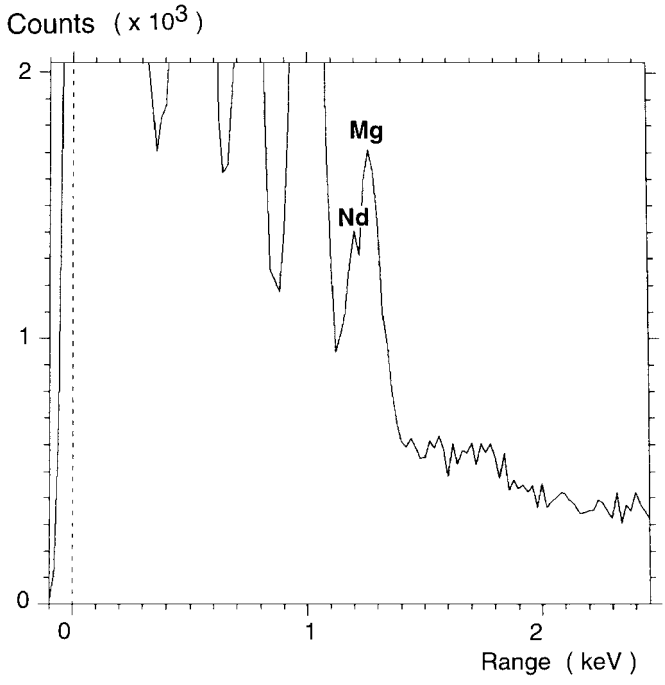

FIG. 15. EDX spectrum obtained from a disordered region of neodymia in the sample loaded with 10 at.% MgO.

Although the effect is difficult to quantify, these materials show an increase in disorder over the pure Nd_2O_3 catalyst. The increased level of performance at higher doping levels ($\geq$3 at.%) is almost certainly due to (a) the dissolution of Mg^{2+} up to 2.5 at.% in the disordered regions of individual Nd_2O_3 grains and (b) the appearance of discrete MgO particles decorated with disordered neodymia thin films (also probably incorporating dissolved Mg^{2+}). Series B doped materials display a notable increase in activity and C_2 selectivity to the extent that at a loading of 10 at.% MgO, the specific activity improves by more than three times and the C_2 selectivity almost sevenfold. This appears to be in direct relation to the presence of an increasing amount or disordered platelike material and significant amounts of discrete MgO particles decorated with disordered thin films of neodymia. The latter morphology is observed frequently in the Series B samples containing 3 and 10 at.% MgO. As with the Series A catalysts, EDX microanalysis shows that the dissolution of magnesium ions in the disordered Nd_2O_3 phase takes place up to 2.5 at.%. Thus, a synergy between MgO and Nd_2O_3 in the OCM reaction has been clearly demonstrated, an effect that can be correlated with physical observations; i.e., the reaction is structure sensitive. It is highly significant that EDX analyses prove that dissolution of Mg^{2+} ions in the neodymia lattice has occurred since this is likely to generate additional O^{2-} vacancy sites which are thought to be beneficial in improving OCM selectivity.

What is more difficult to reconcile is the disparate catalytic performance between Series A and B catalysts when the microstructures of the doped samples containing 3 at.% magnesia are so similar. One possible explanation appears to be related to the observation of fewer discrete MgO particles in Series A catalysts, especially as EDX microanalysis indicates that Mg^{2+} dissolution is comparable for both series of samples. A greater MgO deficiency in Series A catalysts is perfectly plausible given that the coprecipitation process requires that all starting materials are in solution; i.e., dilution of the intended concentration of dopant could take place during catalyst preparation.

5. CONCLUSIONS

It is apparent there are complicated factors to consider in a structure/activity analysis of mixed Nd_2O_3/MgO materials. For instance, there is the tendency of neodymia to hydrate and carbonate (resulting in significant structural disorder) and the unquantified effect that dissolved Mg^{2+} may have in stabilising other neodymium-containing phases. However, for both series of catalysts we believe that in order to achieve good methane coupling performance it is desirable to have the combined effects of disordered neodymia (which we have found to increase as the MgO concentration increases) and discrete MgO particles decorated with disordered neodymia thin films. We also believe the synergy observed is directly linked to the dissolution of Mg^{2+} ions in regions of disordered neodymia. The catalytic performance of the Series B catalysts in particular show these characteristics convincingly as the MgO loading increases. Although Series A catalysts do not show similar dramatic improvements in catalytic performance a synergistic effect is still evident. Hence, we can relate the results from this study directly to those of the Nd_2O_3-doped MgO catalyst system (8) where it was concluded that disordered thin surface Nd_2O_3 films (incorporating dissolved Mg^{2+}) were the most likely source of the observed synergy.

ACKNOWLEDGMENTS

We thank EPSRC for their financial support. We are also indebted to Dr. C. Rhodes for his assistance in the XRD analysis and Mr. P. Shiryaev for his efforts in catalyst preparation.

REFERENCES

1. Kalenik, Z., and Wolf, E. E., *Catal. Spec. Period. Rep. R. Soc. Chem.* **10**, 154 (1993).
2. Hargreaves, J. S. J., Hutchings, G. J., Joyner, R. W., and Kiely, C. J., *J. Catal.* **135**, 576 (1992).
3. Hargreaves, J. S. J., Hutchings, G. J., Joyner, R. W., and Kiely, C. J., *Catal. Today* **13**, 401 (1992).
4. Ito, T., and Lunsford, J. H., *Nature (London)* **314**, 721 (1985).
5. Sinev, M. Yu., Tulenin, Yu. P., and Rozentuller, B. V., *Kinet. Katal.* **32**, 896 (1991).
6. Filkova, D. G., Petrov, L. A., Sinev, M. Yu., and Tulenin, Yu. P., *Catal. Lett.* **13**, 323 (1992).

7. Burrows, A., Blick, K. H., Devenish, R. W., Hutchings, G. J., Joyner, R. W., Kiely, C. J., and Sinev, M. Y., *Stud. Surf. Sci. Catal.* **81**, 223 (1994).
8. Burrows, A., Kiely, C. J., Joyner, R. W., Hutchings, G. J., and Sinev, M. Y., *J. Catal.* **167**, 77 (1997).
9. Zacariasen, W. A., *Acta Crystallogr.* **1**, 265 (1948).
10. Beall, G. W., Milligan, W. O., and Wolcott, H. A., *J. Inorg. Nucl. Chem.* **39**, 65 (1977).
11. Bernal, S., Botana, F. J., Garcia, R., and Rodriguez-Izquierdo, J. M., *React. Solids* **4**, 23 (1987).
12. Bernal, S., Botana, F. J., Garcia, R., and Rodriguez-Izquierdo, J. M., *Ultramicroscopy* **34**, 60 (1990).
13. Bernal, S., Botana, F. J., Calvino, J. J., Cifredo, G. A., Garcia, R., and Rodriguez-Izquierdo, J. M., *J. Chem. Soc. Dalton Trans.*, 1765 (1988).
14. Burrows, A., Ph.D. Thesis, University of Liverpool, 1995.
15. Eyring, L., *in* "Handbook on the Physics and Chemistry of the Rare Earths" (G. A. Gschneider and L. Eyring, Eds.), Chap. 27. North-Holland, Amsterdam, 1979.
16. Warshaw, I., and Roy, R., *J. Phys. Chem.* **65**, 2408 (1961).
17. Stecura, S., U.S. Bureau of Mines Report of Investigations No. 6616, U.S. Department of the Interior, 1965.
18. Le Van, T., Che, M., Kermarec, M., Louis, C., and Tatibout, J. M., *Catal. Lett.* **6**, 395 (1990).
19. Greis, O., *J. Solid State Chem.* **34**, 39 (1980).